ARTICLE

Corrected: Publisher Correction

https://doi.org/10.1038/s41586-018-0850-3

Damage-tolerant architected materials inspired by crystal microstructure

Minh-Son Pham[1]*, Chen Liu[1], Iain Todd[2] & Jedsada Lertthanasarn[1]

Architected materials that consist of periodic arrangements of nodes and struts are lightweight and can exhibit combinations of properties (such as negative Poisson ratios) that do not occur in conventional solids. Architected materials reported previously are usually constructed from identical 'unit cells' arranged so that they all have the same orientation. As a result, when loaded beyond the yield point, localized bands of high stress emerge, causing catastrophic collapse of the mechanical strength of the material. This 'post-yielding collapse' is analogous to the rapid decreases in stress associated with dislocation slip in metallic single crystals. Here we use the hardening mechanisms found in crystalline materials to develop architected materials that are robust and damage-tolerant, by mimicking the microscale structure of crystalline materials—such as grain boundaries, precipitates and phases. The crystal-inspired mesoscale structures in our architected materials are as important for their mechanical properties as are crystallographic microstructures in metallic alloys. Our approach combines the hardening principles of metallurgy and architected materials, enabling the design of materials with desired properties.

A crystal is composed of atoms that are arranged in an ordered manner in space. The ordered arrangement of atoms is called the crystal lattice, and is defined by a unit cell (Fig. 1a)—the smallest group of lattice points that can describe the overall symmetry of the crystal. A single crystal consists of unit cells of the same type and orientation, but most crystalline materials consist of many domains, each of which contains a lattice orientation that is different from those of its neighbours. Such domains are separated by boundaries and, in the context of metallurgy, are referred to as crystal grains. Crystalline materials consisting of many crystal grains are called polycrystals. In addition to the crystal lattice, there are other features of the crystallographic microstructure (such as dislocations, grains, phases and precipitates) that can be manipulated to control the plastic deformation of crystals under external load[1,2].

The most common mechanism responsible for plastic deformation is the slip of dislocations[1]. For single crystals, a dominant, single slip mode occurs during plastic deformation (Fig. 1b)[3], which causes the strain to become localized and the stress required for further deformation to decrease[4]. For polycrystals, the change in lattice orientation across grain boundaries can impede or even stop dislocations moving from one grain to the next (Fig. 1c)[5], resulting in grain-size-dependent plastic deformation[4]. This capacity to constrain deformation and prevent the rapid propagation of slip minimizes the decreases in stress[6] and strengthens polycrystals[1]. The size of the grains can greatly alter the mechanical strength, as described by the Hall–Petch relationship[7–9], which states that the yield strength (σ_y) of polycrystals is inversely proportional to the square-root of the grain size (d):

$$\sigma_y = \sigma_0 + \frac{k}{\sqrt{d}} \quad (1)$$

where σ_0 is the frictional stress, which does not depend on the grain size, and k is a material constant.

Precipitates and phases similarly control slip in crystals, owing to the difference in lattice parameters, leading to other strengthening sources in crystalline alloys—termed precipitation and phase hardening in metallurgy[1]. The capacity to control the strength and toughness of alloys by engineering the size, distribution and orientation of grains, precipitates and second phases forms the foundation of physical metallurgy.

Similarly to the mimicry of structures inside biological systems (or organic materials) to design bio-inspired materials[10–13], we mimic the crystal microstructure of metals and alloys on a macroscopic scale by constructing a lattice unit cell that consists of an ordered arrangement of nodes (analogous to atoms) connected by struts (equivalent to atomic bonds) (Fig. 1d). Architected lattice materials may then be straightforwardly generated from a macroscale lattice unit in space using a computer-aided design package and fabricated via additive manufacturing (also termed 3D printing). As for crystals, the properties of architected materials are strongly affected by their lattice architecture[14]. The behaviour of architected lattices can be modified through careful design of the lattice unit cells, giving access to unprecedented properties, such as very low mass with high specific strength[15,16] and negative Poisson ratio[17,18]. Further, by manufacturing the lattices using different materials, architected materials have been developed that are lightweight and strong[19]. However, work on such architected materials has so far focused only on lattice materials with a single orientation[14,16,20,21], which have been observed to suffer the same collapse of mechanical strength when loaded beyond the yield point as occurs in single crystals. This 'post-yielding collapse' is due to the occurrence of shear bands[21] (Fig. 1f), which cause deformation to become highly localized on specific planes with defined lattice directions[21,22]. This behaviour is similar to the slip along defined planes and directions, and to the rapid decreases in stress induced by the slip activity in single crystals (compare Fig. 1e, f and Fig. 1b).

Given the similarity between single crystals and singly oriented lattice structures, we posited that it should be possible to develop damage-tolerant architected materials by introducing hardening mechanisms analogous to those found in crystalline materials. Our proposal is related to a recent approach that aims to combine the component structure design and metallurgy by reducing the component

[1]Department of Materials, Imperial College London, London, UK. [2]Department of Materials Science and Engineering, University of Sheffield, Sheffield, UK. *e-mail: son.pham@imperial.ac.uk

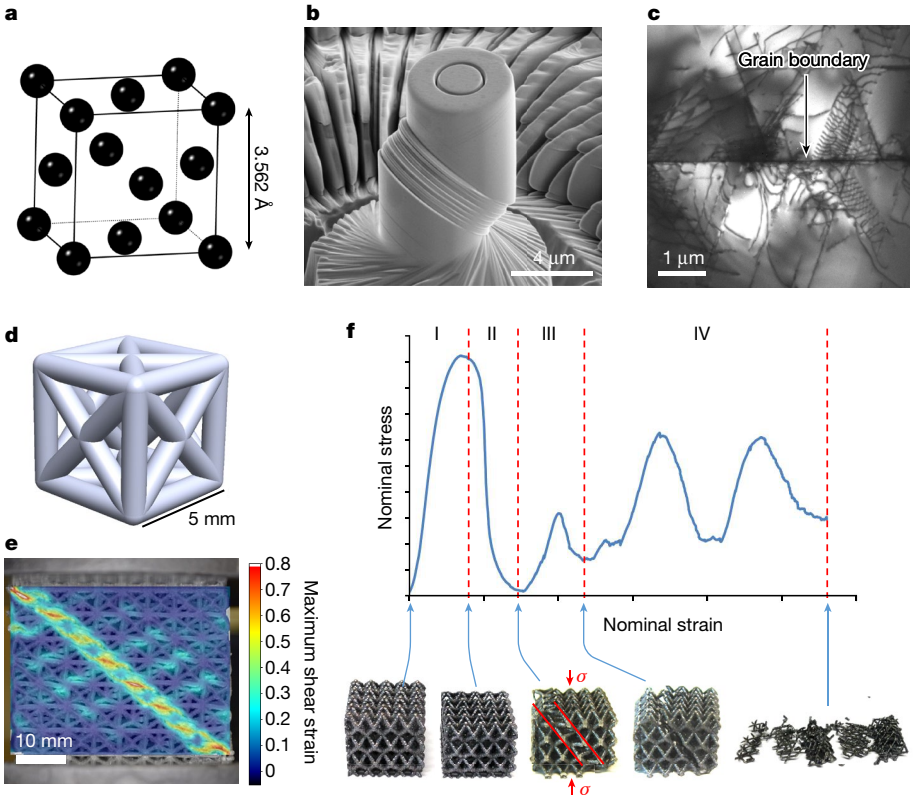

Fig. 1 | Lattice structures and deformation behaviour. a, Face-centred cubic (fcc) crystal lattice of iron. **b**, Dislocation slip in a single crystal. Image reproduced with permission from ref. [3], Elsevier. **c**, Dislocation slip at a grain boundary in a polycrystalline steel. Image reproduced with permission from ref. [5], Elsevier. **d**, Architected fcc lattice. **e**, Single slip in a singly oriented lattice; the colour represents the degree of maximum shear strain. **f**, Unstable stress–strain behaviour often seen in architected metallic lattices: region I, elastic deformation; region II, abrupt decrease in stress because of the occurrence of a shear band (the location of the first shear band is highlighted by two parallel red lines in the middle inset at the bottom; σ is the applied stress; the arrows show the loading direction); region III, stress increase due to the densification and another drop in stress, due to the occurrence of another shear band; region IV, intermittent increases and decreases in stress due to the occurrence of shear bands. Image adapted from ref. [21], which is published under a CC BY 4.0 licence (https://creativecommons.org/licenses/by/4.0/).

size to closer to that of metallurgical microstructures[11,23]. However, it is distinct because it involves mimicking crystallographic microstructure on a macro- or mesoscale to enable the combination of metallurgical hardening mechanisms and architected materials. Here, we present a method for designing mesoscale lattice features that mimic crystallographic microstructure, to integrate metallurgical hardening principles (grain-size effect, precipitation and multiphase hardening) into the development of architected materials. We demonstrate that crystal-inspired mesostructures strengthen the architected materials, leading to highly damage-tolerant materials. The freedom in designing crystal-like mesostructures also provides alternative ways of studying complex metallurgical phenomena (such as slip transfer) in metallic alloys. We further show that fabricating lattices using polycrystalline materials leads to hierarchical architected materials, which contain atomic lattices within mesoscale architected lattices and polycrystal microstructure within polycrystal-like mesostructure. The properties of these materials may easily be tailored via the numerous combinations of micro-, meso- and macro-scale lattices.

Grain-boundary hardening

Tailoring the misorientation between two adjoining macro-lattice domains creates a boundary between them similar to the boundary between two adjoining crystal grains (Methods subsection 'Mimicking polygrains'). Hereafter, each domain of the same lattice orientation is termed a meta-grain. Because atoms can bond with new neighbouring atoms whereas physical nodes cannot, there is a clear difference between polycrystals and polycrystal-inspired materials. As an initial step, we chose two well understood phenomena in metallurgy to verify whether relationships observed in polycrystals are applicable to architected materials with polycrystal-like features: (i) symmetric slip in a twinned bi-crystal (Fig. 2a)[24] and (ii) the Hall–Petch relationship[7,8].

To investigate phenomenon (i), we designed and 3D-printed an architected material containing two meta-grains separated by a twin boundary (Methods subsection 'Mimicking polygrains'; Extended Data Figs. 1, 2a, b). The base material used to fabricate the twinned meta-grains was an elasto-plastic polymer (Methods section 'Materials and fabrication'). Later in this section, we demonstrate that a polycrystal-inspired architected material fabricated using different base materials (including a stainless steel) exhibits the same behaviour in forming shear bands, demonstrating the wide applicability of our polycrystal-inspired approach. Under compression, with the loading parallel to the twin boundary, shear bands occurred and were parallel to the planes of maximum shear stress (Fig. 2b). In addition, we observe that the shear bands that form are symmetric about the twin boundary, confirming that the shear-band behaviour in meta-grain twins is similar to the slip activity in crystal twins (Fig. 2a, b).

To assist us in understanding this behaviour, we used finite-element modelling (FEM) to simulate the early stage of shear-band formation (Methods). The simulation predicts well the location and direction of shear bands in meta-grain twins seen in the experiment (Fig. 2c). By design, the (001) plane in each meta-grain was parallel to the maximum shear force in that meta-grain domain. FEM shows that, as expected, deformation occurred via the buckling of ⟨001⟩ struts between two parallel (001) planes and along a ⟨101⟩ direction, leading to a shear band through the face-centred nodes parallel to the (001) plane of the face-centred cubic (fcc) lattice (Supplementary Video 1). The family of shear bands with directions ⟨101⟩ and planes {002} is different from the slip family in fcc crystals (with directions ⟨101⟩ and planes {111}), highlighting one of the

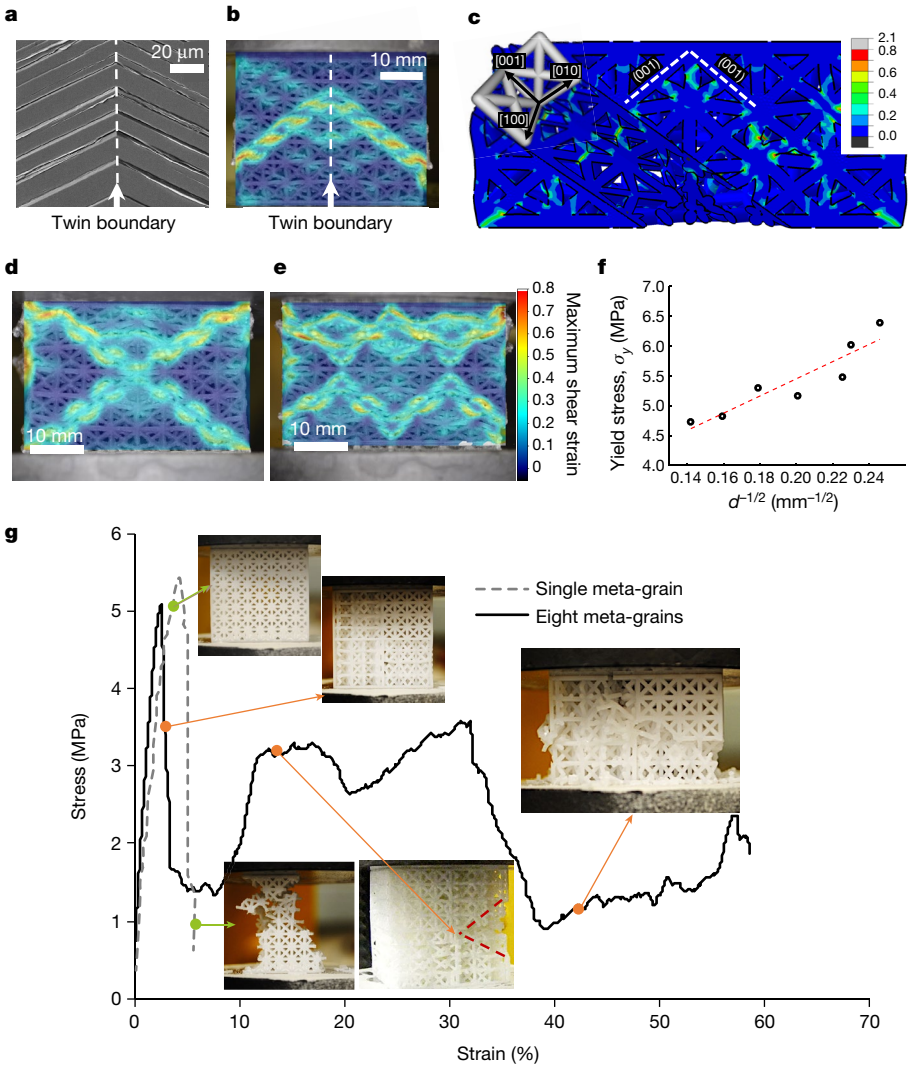

Fig. 2 | Role of lattice orientation in the deformation behaviour of crystals and architected lattices. a, Twinned bi-crystal. Image reproduced with permission from ref. [24], Elsevier. **b**, **c**, Shear bands in meta-grain twins observed in experiment (**b**) and predicted by FEM (**c**). The cut sections formed from cutting planes parallel to the (100) and (010) planes of the fcc architected lattice show the deformation of internal struts; dashed lines trace the (001) plane. The colour scale shows the maximum principal logarithmic strain, which was averaged at nodes common to two or more elements when the relative difference between contributions from the elements was smaller than 75%. **d**, **e**, Shear bands were controlled by changing the orientation of the meta-grains: eight meta-grains (**d**) and 16 meta-grains (**e**). The nominal strain was 30%. **f**, Yield strength σ_y versus the size of the meta-grains d. The dashed red line is a linear fit to the experimental data (black circles): $\sigma_y = 2.58 + 14.37d^{-1/2}$. **g**, Boundaries between meta-grains effectively stop cracks in brittle lattices (see dashed red lines in the bottom right inset), leading to a substantial increase in the toughness of the architected materials (the area below the stress–strain curve defines the energy absorption per unit volume, or toughness). The insets show snapshots of the architected materials at given strains.

differences between the fcc crystal lattice and the architected lattice. The symmetry of the lattice orientation across the boundary causes the same localization parallel to the (001) plane in the other meta-grain, resulting in symmetric shear bands in the twinned meta-grains.

The twin boundary was also used to increase the number of meta-grains, in essence by reducing the size of the meta-grains (Methods subsection 'Mimicking polygrains'; Extended Data Fig. 2), to study phenomenon (ii) in the architected materials. Fabricated polycrystal-like materials demonstrated highly reproducible constitutive stress–strain behaviour (Extended Data Fig. 3). The change in orientation across boundaries effectively controls the propagation of shear bands (Fig. 2b, d, e). Most importantly, the yield strength of architected materials substantially increases with the reduction in the meta-grain size (Fig. 2f, Extended Data Fig. 4a). This result confirms that an effect similar to the Hall–Petch relationship exists for the architected materials. Fitting against experimental data using equation (1) gives $\sigma_0 = 2.58$ MPa and $k = 14.37$ MPa mm$^{1/2}$. The value of k falls well in the range for conventional polycrystalline metals[25].

The flow stress at a given strain is also observed to increase with the reduction in the meta-grain size during plastic deformation (Extended Data Fig. 4b). In other words, the size of meta-grains strongly affects both the yield strength and the work-hardening during the deformation of architected materials. This observation of the size effect (together with the deflecting effect; Fig. 2b, d, e) is important, because it confirms that the boundary strengthening is applicable to architected materials. The grain-size dependence in polycrystals is one of the most widely used mechanisms in metallurgy to achieve both strength and ductility; for example, a tough steel was developed via the ultra-refinement of grains for low-temperature applications[26]. However, the grain-size effect in metals would be much more substantial in the presence of incoherent high-angle boundaries[27]. This indicates that reducing the size of high-angle boundaries might substantially strengthen architected materials. With the freedom to vary the size while keeping the same type of boundary, our approach can provide clean data (related to the size effect only, without interference associated with the type of boundary) and thus insights into the grain-size effect of a specific type

of boundary. Obtaining clean data in metallurgy is not possible because there are no effective ways of reducing the grain size while maintaining the same (single) type of grain boundary. The physical metallurgy of polycrystals thus provides the underlying science for engineering architected materials; our polycrystal-inspired approach offers alternative ways of studying complex phenomena in metallurgy.

Metallurgical studies suggest that microstructure (such as dislocation substructures and high-angle boundaries) may even be able to stop the propagation of short cracks[28–30]. We fabricated a series of samples from a different base material to study the effect of incoherent high-angle boundaries on crack propagation in architected materials (Methods section 'Materials and fabrication'; Extended Data Table 1). The base material used for these architected materials is a brittle polymer, so cracks are easily generated under loading. For a singly oriented lattice, cracks occurred and propagated rapidly throughout the macro-lattice, causing premature and fast fracture (Fig. 2g, dashed line). For the architected material containing eight meta-grains with incoherent high-angle boundaries (Fig. 2g, solid line; Extended Data Fig. 5), the rotation of the orientation of the internal lattice led to the creation of incomplete unit cells on the free surface, resulting in a lower yield strength compared to the singly oriented lattice. Nevertheless, cracks did stop at the incoherent high-angle boundaries, preventing fast brittle fracture (Fig. 2g, solid line). It is well known in metallurgy that crystallographic microstructure is able to stop and deflect the propagation of cracks when the size of the microstructure is comparable to the crack length[28,29]. Mimicking microstructure at the macroscale makes polycrystal-like structures comparable to macroscale cracks. The change in lattice orientation across incoherent high-angle boundaries stops the propagation of cracks. In addition, owing to the presence of these boundaries, the architected material retained its strength after yielding and was able to carry load up to large deformation, substantially improving the energy absorption of the material (Fig. 2g) from about 194 kJ m^{-3} for the singly oriented lattice to about 1,309 kJ m^{-3} for the polycrystal-like material. This large increase in the energy absorption associated with the presence of incoherent high-angle boundaries is in agreement with a widely accepted approach used to strengthen alloys—grain boundary engineering[26].

To study the influence of the base material on the behaviour of polycrystal-like architected materials, we 3D-printed the same architected material (containing eight meta-grains with incoherent high-angle boundaries) using two other base materials (an elasto-plastic polymer and an austenitic stainless steel; Methods section 'Materials and fabrication'). We find that the choice of base material does affect the behaviour of the macro-lattices. In contrast to the lattice made from the brittle polymerization resin, there were no brittle cracks in the lattices made from the elasto-plastic polymer and the steel, owing to the intrinsic ductility of these materials. However, the localization of strain in the polymer lattice is very similar to that in the steel lattice (Extended Data Fig. 6a, b). The localized deformation of struts led to the formation of shear bands in the 30°- and 60°-oriented meta-grains in both the ductile polymer and the metallic lattices (Extended Data Fig. 6a, b). The change in orientation altered the localization in the architected lattices fabricated from the two alternative base materials, confirming that our crystal-inspired approach is widely applicable to various materials.

In contrast to the shear-band activity, which is governed mainly by the lattice architecture, the constitutive stress–strain behaviour is strongly affected by the base material because different base materials have different yield strengths and work-hardening behaviour. The metallic lattice undergoes substantial hardening during plastic deformation, much more than does the polymer lattice (Extended Data Fig. 6c, d), because the metallic base material itself hardens during deformation owing to the change in its intrinsic microstructure (in particular, the arrangement and density of dislocations)[31]. Consequently, the application of boundary hardening to metallic base materials enables the synergistic strengthening associated with both crystallographic microstructures and designed mesostructures.

Precipitation hardening

Precipitation hardening is widely used in metallurgy to design and manufacture high-performance alloys, such as nickel-based superalloys[32]. In precipitate-hardened alloys, precipitates act as obstacles to the movement of dislocations. The influence of precipitates on the strength of alloys depends on the size, shape, volume fraction and distribution of precipitates, and on the coherency between the precipitates and the matrix[33]. We incorporated precipitation strengthening into our lattice design by introducing embedded lattice domains (termed meta-precipitates) with different lattice parameters from those of the matrix. The lattice parameters (type, spacing and orientation) of meta-precipitates can be tailored to assign different degrees of coherency between the meta-precipitates and the matrix. In addition, the diameters of the struts in the meta-precipitates can be varied to account for different 'atomic bond' strengths, such as the Ni–Al and Al–Al bonds in the ordered Ni_3Al (γ' $L1_2$) crystal phase in nickel superalloys[32].

We 3D-printed a single fcc architected material containing face-centred tetragonal meta-precipitates that were stronger than the matrix owing to shorter lattice spacing (Extended Data Fig. 7). These lattices demonstrate highly reproducible behaviour (Extended Data Fig. 8). It appears that the harder meta-precipitates restrict and control the shear-band propagation (compare Fig. 3a with Fig. 3c, d), stabilizing the overall lattice and substantially strengthening the overall architected materials (Fig. 3b). Shear bands were stopped at and bowed around the interfaces between the meta-precipitates and the matrix (Fig. 3d). This governing effect on the meta-precipitates is similar to the Orowan hardening effect, in which the strength of crystals containing precipitates is proportional to the strength of the precipitates and the spacing between precipitates[33,34]. This parallel between architected materials (containing meta-precipitates) and alloys (containing precipitates) means that the mechanical response of architected materials may be readily manipulated by varying the lattice parameters and the volume fraction and distribution of meta-precipitates.

Multi-phase hardening

In multi-phase metals, such as martensitic stainless steels, hard phases provide high strength to enhance load-bearing capacity whereas soft phases accommodate plastic deformation. Because a crystal phase is defined by its lattice type, multiple phases can be imitated by assigning different lattice types to different macro-lattice domains. We designed an architected material comprising two phases (fcc in the top and bottom layers and body-centred cubic (bcc) in the middle layer; Extended Data Fig. 9). Because the unit cell of the fcc macro-lattice has a higher connectivity and higher density than the bcc architected phase, the fcc architected phase is stronger than the bcc one (Fig. 3e, solid and dashed grey lines). Similarly to the behaviour of soft–hard multiphase crystals, the strength of the multi-phase architected material results mainly from the strength of the hard fcc phase (Fig. 3e, black and grey solid lines), whereas plastic deformation was accommodated mainly by the soft bcc meta-grains, resulting in the confinement of shear bands mainly to the middle layer (Fig. 3e, top left inset). Therefore, the mixture of hard and soft architected phases provides additional means of tailoring the properties of and controlling shear bands along specific paths inside architected materials.

Taking this one step further, some highly engineered alloys can also exhibit a solid-state phase transformation, whereby the crystal structure transforms via the rearrangement of atoms in the unit cell under external loads. In some cases, reversible phase transformations lead to a shape memory effect and superelasticity[35]. To see whether such a transformation is possible in crystal-inspired materials, we designed a Kresling lattice[36] to loosely mimic a hexagonal close-packed (hcp) phase (Extended Data Fig. 10). Under compression, the Kresling lattice twisted as a result of bending and local buckling of struts on prismatic and basal planes (Fig. 3g; Supplementary Videos 2, 3), causing helical movement of the nodes (Extended Data Fig. 11). This movement of the nodes altered their arrangement, enabling a 'phase transformation'. Accurately mimicking a specific type of phase transformation

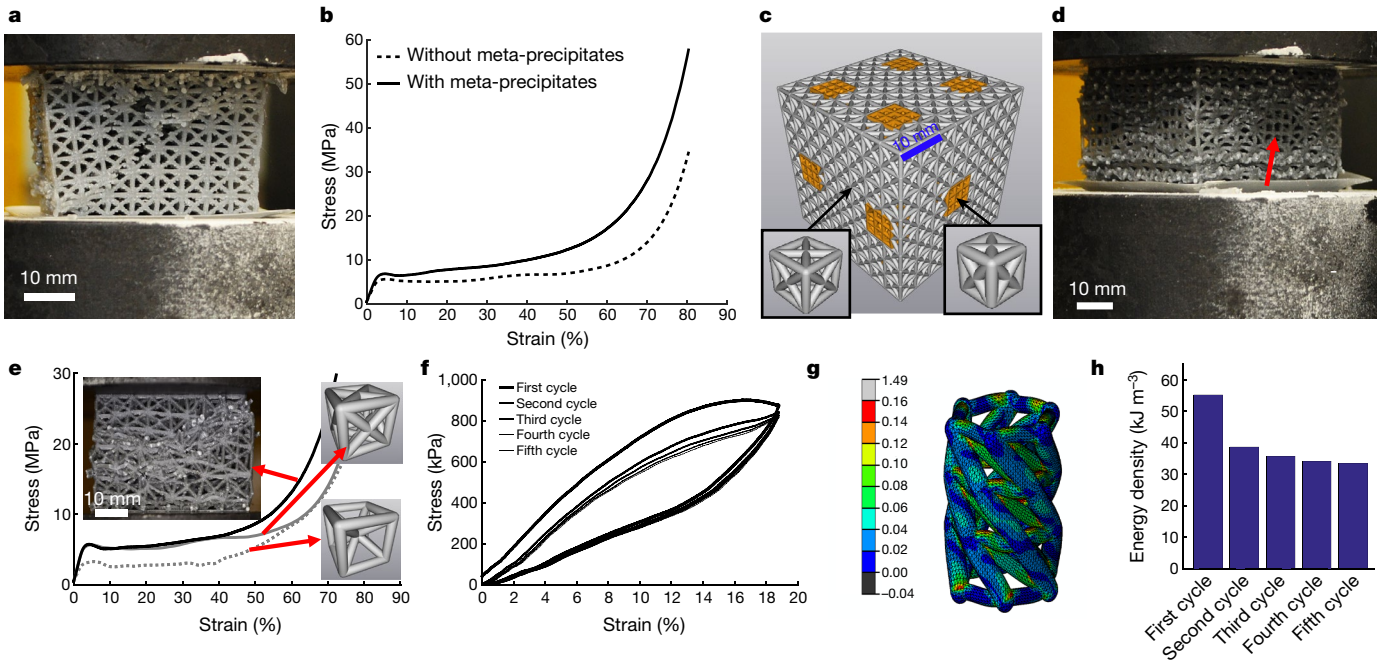

Fig. 3 | Precipitation and multiphase hardening in architected materials. a, Deformation of a singly oriented lattice without meta-precipitates at an engineering strain of 27%. **b**, Constitutive stress–strain responses of architected materials without (see **a**) and with (see **c** and **d**) meta-precipitates. **c**, **d**, Schematic (**c**) and image (**d**) of an architected material containing face-centred tetragonal meta-precipitates (right inset in **c**). The red arrow in **d** highlights a meta-precipitate; engineering strain is 36%. In **a**–**d**, the matrix lattice was built from an fcc unit cell (see left inset in **c**). **e**, Mechanical behaviour of single-phase (grey solid line, fcc; grey dotted line, bcc; see two right insets) versus multiphase (black line; see left inset) architected materials. **f**, Pseudo-superelasticity exhibited in the first five loading–unloading cycles of the Kresling lattice. **g**, FEM simulation showing the strain localization and local buckling of struts; colour scale as in Fig. 2c. **h**, Energy per unit volume of the first five loading–unloading cycles.

in crystals requires only some additional design calculations of the helical movement of nodes to enable the change in the stacking sequence (such as ABABAB to ABCABC for the hcp-to-fcc transformation[37]). The transformed phase was not stable during unloading, but it should be straightforward to generate a lattice structure that is stable in both the original and the transformed configuration, for example, by incorporating the design of multi-stable cellular structures[38,39].

The transformation back to the original arrangement upon unloading leads to pseudo-superelasticity (Fig. 3f). The observed changes in the elastic modulus (Fig. 3f) are a result of a change from overall elastic bending to local buckling of struts on the prismatic planes (Fig. 3g). The increasing compressional load caused a gradual transition from overall elastic bending to local buckling of struts near basal nodes. During unloading, the decreasing load led to a more abrupt change: struts unbuckled at more defined strains (from 14% to 12% during unloading), leading to a change in the bending moment. Such a change caused different friction on the interacting faces between the Kresling lattice and the compressing plates, resulting in energy dissipation during transformation (Fig. 3h). This reversible alternation of node arrangements demonstrates that phase transformations can be mimicked in architected phases, opening up the possibility of making lattices with high energy absorption: external work can be dissipated by a phase transformation, and the lattice then returns to its original shape via the reverse transformation upon unloading.

Multiscale hierarchical crystal structures

By combining all sources for tailoring the properties of architected materials containing crystal-like mesostructures, it will be possible to design lightweight components in which the mesostructures respond better to external loads, or to direct the accumulated damage (shear bands and cracks) along specific structural paths as desired (Fig. 4a–d). By using a crystalline material to fabricate crystal-like architected materials (e.g., Extended Data Fig. 6a, c), we generate architected materials that have a multiscale, hierarchical crystal structure, consisting of crystallographic microstructures at the micrometre scale, which are mimicked and repeated in crystal-inspired mesostructures at the millimetre scale (or larger depending on the build volume, which varies for different manufacturing methods). In other words, each architected material contains micro-crystals within macro-crystals; for example, a millimetre-sized fcc architected material (Fig. 4e) contains an atomic fcc lattice (Fig. 4g), and a centimetre-sized architected polygrain macrostructure (Fig. 4d) is made up of micrometre-sized intrinsic polygrain microstructures of an austenitic stainless steel (Fig. 4f). A hierarchical superlattice can be generated similarly, by using a nickel superalloy to fabricate an architected meso-lattice that mimics the γ/γ' superlattice found in nickel superalloys (Fig. 4h; note that different diameters and lengths need to be used for specific struts in the meta-precipitates to mimic the ordered Ni–Al atomic bonds in the γ'-Ni_3Al phase). Such multiscale hierarchical crystal structures do not occur in nature, meaning that the architected materials are a type of meta-material; we refer to them as meta-crystals. The architected lattice mesostructures can be changed by design, and the atomic-scale crystal lattices and crystal microstructure can readily be changed, for example, by changing the base material. Consequently, it is possible to engineer hierarchical lattices across multiple length scales. As discussed previously, the use of crystalline alloys enables the synergistic strengthening associated with both crystal microstructures and crystal-inspired meso- and macrostructures. The interplay between microstructure and designed structure at different length scales could uncover new properties and potential applications for this class of materials.

Conclusions

We have presented a way of integrating the hardening mechanisms found in crystalline alloys into architected materials, enabling the design of materials with desired properties. We carried out a comprehensive study to substantiate: (1) the similarities between shear bands in crystal-inspired architected materials and dislocation slip in

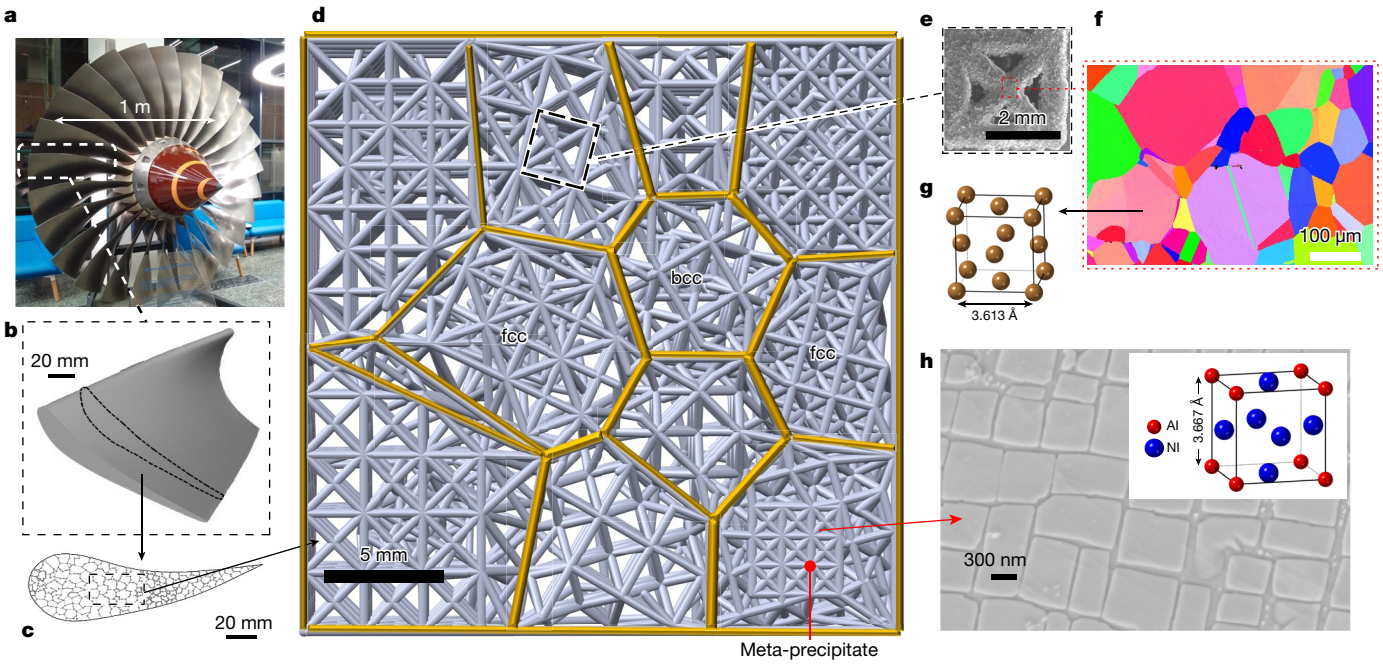

Fig. 4 | Lightweight and damage-tolerant architected materials inspired by crystal microstructure. a–d, Lightweight lattice components: a fan in an aeroplane engine (**a**) consists of many blades (**b**), which each contain multiple cellular domains (**c**) that are filled with crystal-inspired mesolattice features (**d**). **e–g**, Hierarchical fcc lattices from the atomic scale up to centimetre scales: the architected lattice (**e**) consists of fcc polygrains (**f**; each individually coloured), each of which was built from an fcc unit cell of atoms (**g**). **h**, Intrinsic γ/γ' microstructure in nickel superalloys; the inset illustrates the unit cell of the γ' phase.

crystals, and (2) the applicability of various strengthening mechanisms (grain-boundary, precipitation and multiphase strengthening) to architected materials. Our study confirms that metallurgical concepts can be applied to enhance the mechanical behaviour of architected materials. In return, our crystal-inspired approach provides alternative ways of studying complex phenomena in metallurgy. The combination of physical metallurgy and architected meta-materials opens up new opportunities for: (1) designing and engineering damage-tolerant architected materials with desired strength and toughness, and (2) enhancing the functionality and performance of architected materials in response to external loads. The possibilities offered by our approach are not limited to those presented here; the application of our approach to crystalline metallic alloys will lead to new experimental and computational research which will improve our understanding of the possibilities afforded by varying both the intrinsic microstructure and the designed mesostructure of meta-crystals.

Online content

Any methods, additional references, Nature Research reporting summaries, source data, statements of data availability and associated accession codes are available at https://doi.org/10.1038/s41586-018-0850-3.

Received: 29 March 2018; Accepted: 29 November 2018;
Published online 16 January 2019.

1. Cottrell, A. *Dislocations and Plastic Flow in Crystals* (Clarendon Press, New York, 1953).
2. Argon, A. *Strengthening Mechanisms in Crystal Plasticity* (Oxford Univ. Press, New York, 2007).
3. Dimiduk, D. M., Uchic, M. D. & Parthasarathy, T. A. Size-affected single-slip behavior of pure nickel microcrystals. *Acta Mater.* **53**, 4065–4077 (2005).
4. Csikor, F. F., Motz, C., Weygand, D., Zaiser, M. & Zapperi, S. Dislocation avalanches, strain bursts, and the problem of plastic forming at the micrometer scale. *Science* **318**, 251–254 (2007).
5. Pham, M. S., Holdsworth, S. R., Janssens, K. G. F. & Mazza, E. Cyclic deformation response of AISI 316L at room temperature: mechanical behaviour, microstructural evolution, physically-based evolutionary constitutive modelling. *Int. J. Plasticity* **47**, 143–164 (2013).
6. Imrich, P. J., Kirchlechner, C., Motz, C. & Dehm, G. Differences in deformation behavior of bicrystalline Cu micropillars containing a twin boundary or a large-angle grain boundary. *Acta Mater.* **73**, 240–250 (2014).
7. Hall, E. O. The deformation and ageing of mild steel: III. Discussion of Results. *Proc. Phys. Soc. B* **64**, 747–753 (1951).
8. Petch, N. J. The cleavage strength of polycrystals. *J. Iron Steel Inst.* **174**, 25–28 (1953).
9. Subedi, S., Beyerlein, I. J., LeSar, R. & Rollett, A. D. Strength of nanoscale metallic multilayers. *Scr. Mater.* **145**, 132–136 (2018).
10. Wegst, U. G. K., Bai, H., Saiz, E., Tomsia, A. P. & Ritchie, R. O. Bioinspired structural materials. *Nat. Mater.* **14**, 23–36 (2015).
11. Barthelat, F. Architectured materials in engineering and biology: fabrication, structure, mechanics and performance. *Int. Mater. Rev.* **60**, 413–430 (2015).
12. Chen, P.-Y., McKittrick, J. & Meyers, M. A. Biological materials: functional adaptations and bioinspired designs. *Prog. Mater. Sci.* **57**, 1492–1704 (2012).
13. Gu, G. X., Libonati, F., Wettermark, S. D. & Buehler, M. J. Printing nature: unraveling the role of nacre's mineral bridges. *J. Mech. Behav. Biomed. Mater.* **76**, 135–144 (2017).
14. Gibson, L. J. & Ashby, M. F. *Cellular Solids: Structure and Properties* (Cambridge Univ. Press, Cambridge, 1997).
15. Schaedler, T. A. & Carter, W. B. Architected cellular materials. *Annu. Rev. Mater. Res.* **46**, 187–210 (2016).
16. Schaedler, T. A. et al. Ultralight metallic microlattices. *Science* **334**, 962–965 (2011).
17. Lakes, R. Foam structures with a negative Poisson's ratio. *Science* **235**, 1038–1040 (1987).
18. Andreassen, E., Lazarov, B. S. & Sigmund, O. Design of manufacturable 3D extremal elastic microstructure. *Mech. Mater.* **69**, 1–10 (2014).
19. Qin, Z., Jung, G. S., Kang, M. J. & Buehler, M. J. The mechanics and design of a lightweight three-dimensional graphene assembly. *Sci. Adv.* **3**, e1601536 (2017).
20. Zheng, X. et al. Multiscale metallic metamaterials. *Nat. Mater.* **15**, 1100–1106 (2016); addendum **16**, 497 (2017).
21. Qiu, C. et al. Influence of processing conditions on strut structure and compressive properties of cellular lattice structures fabricated by selective laser melting. *Mater. Sci. Eng. A* **628**, 188–197 (2015); corrigendum **638**, 228–231 (2015).
22. Maskery, I. et al. A mechanical property evaluation of graded density Al-Si10-Mg lattice structures manufactured by selective laser melting. *Mater. Sci. Eng. A* **670**, 264–274 (2016).
23. Bouaziz, O., Brechet, Y. & Embury, J. D. Heterogeneous and architectured materials: a possible strategy for design of structural materials. *Adv. Eng. Mater.* **10**, 24–36 (2008).
24. Li, L. L. et al. Microcompression and cyclic deformation behaviors of coaxial copper bicrystals with a single twin boundary. *Scr. Mater.* **69**, 199–202 (2013).
25. Armstrong, R., Codd, I., Douthwaite, R. M. & Petch, N. J. The plastic deformation of polycrystalline aggregates. *Philos. Mag.* **7**, 45–58 (1962).
26. Kimura, Y., Inoue, T., Yin, F. & Tsuzaki, K. Inverse temperature dependence of toughness in an ultrafine grain-structure steel. *Science* **320**, 1057–1060 (2008).

27. Hirth, J. P. The influence of grain boundaries on mechanical properties. *Metall. Trans.* **3**, 3047–3067 (1972).
28. Suresh, S. & Ritchie, R. O. Propagation of short fatigue cracks. *Int. Mater. Rev.* **29**, 445–475 (1984).
29. Pham, M. S. & Holdsworth, S. R. Role of microstructural condition on fatigue damage development of AISI 316L at 20 and 300 °C. *Int. J. Fatigue* **51**, 36–48 (2013).
30. Kobayashi, S., Nakamura, M., Tsurekawa, S. & Watanabe, T. Effect of grain boundary microstructure on fatigue crack propagation in austenitic stainless steel. *J. Mater. Sci.* **46**, 4254–4260 (2011).
31. Pham, M.-S. & Holdsworth, S. Evolution of relationships between dislocation microstructures and internal stresses of AISI 316L during cyclic loading at 293 K and 573 K (20 °C and 300 °C). *Metall. Mater. Trans. A* **45**, 738–751 (2014).
32. Reed, R. C. *The Superalloys: Fundamentals and Applications* Ch. 2 (Cambridge Univ. Press, Cambridge, 2006).
33. Orowan, E. Discussion on internal stresses. In *Symp. Internal Stresses in Metals and Alloys* 451–453 (Inst. of Metals, 1948).
34. Hirsch, P. B. & Humpreys, F. J. The deformation of single crystals of copper and copper-zinc alloys containing alumina particles - I. Macroscopic properties and workhardening theory. *Proc. R. Soc. Lond. A* **318**, 45–72 (1970).
35. Porter, D. A. & Easterling, K. E. *Phase Transformations in Metals and Alloys* (CRC Press, Boca Raton, 2009).
36. Kresling, B. in *Deployable Structures and Biological Morphology* (eds Furuya, H. et al.) 188–195 (Internet-First Univ. Press, Ithaca, 2008).
37. Zhao, H. et al. Atomic-scale understanding of stress-induced phase transformation in cold-rolled Hf. *Acta Mater.* **131**, 271–279 (2017).
38. Shan, S. et al. Multistable architected materials for trapping elastic strain energy. *Adv. Mater.* **27**, 4296–4301 (2015).
39. Restrepo, D., Mankame, N. D. & Zavattieri, P. D. Phase transforming cellular materials. *Extreme Mech. Lett.* **4**, 52–60 (2015).

Acknowledgements M.-S.P. thanks A. Rollett, F. Dunne, C. Gourlay and S. Holdsworth for discussions, T. Walton and P. Hooper for fabricating some lattices, A. Piglione for providing an SEM image of γ/γ' microstructure, and an Engineering Alloys Fellowship awarded by the Department of Materials, Imperial College London. M.-S.P. also thanks M. M. Attallah and D. M. Dimiduk for providing the original versions of Fig. 1b, f. I.T. is grateful for funding through EPSRC grants EP/P006566/1 and EP/L02513/1, and the Royal Academy of Engineering.

Reviewer information *Nature* thanks C. Niordson, N. Pugno and the other anonymous reviewer(s) for their contribution to the peer review of this work.

Author contributions M.-S.P. developed the idea and directed the research. C.L. carried out the computer-aided design, fabrication, mechanical tests and post analyses. J.L. performed the FEM. I.T. discussed and contributed to the development of the concept. All the authors participated in analysing and interpreting the data. The manuscript was written and approved by all authors.

Competing interests A patent developed on the basis of the approach proposed in this study has been filed, managed by Imperial Innovations.

Additional information
Extended data is available for this paper at https://doi.org/10.1038/s41586-018-0850-3.
Supplementary information is available for this paper at https://doi.org/10.1038/s41586-018-0850-3.
Reprints and permissions information is available at http://www.nature.com/reprints.
Correspondence and requests for materials should be addressed to M.-S.P.
Publisher's note: Springer Nature remains neutral with regard to jurisdictional claims in published maps and institutional affiliations.

METHODS

Design. A unit cell of a crystal lattice is defined by the distances between atoms along the three principal axes x, y and z (defined by the lattice constants a, b and c) and the angles between them (Extended Data Fig. 1a). For cubic lattices, $a = b = c$ and the x, y and z axes are parallel to the three [100] orientations of lattice (the angles between which are all 90°). All macroscale fcc unit cells in this study had the same node arrangement and connection as that shown in Extended Data Fig. 1a. We designed and fabricated macroscale cubes containing crystal-like mesostructures to study the roles of such mesostructures in the behaviour of architected materials (Extended Data Fig. 1b). A global (X, Y, Z) coordinate associated with each cube was defined by the three orthogonal directions of the cube (Extended Data Fig. 1b). The global dimensions of our macroscale cubes were 40 mm × 40 mm × 40 mm. All lattice models presented here were designed using software from Solidworks and Element.

Mimicking polygrains. The global cubic matrix was fragmented into Voronoi domains. Each domain mimics a crystalline grain: it is in-filled by a macro-lattice whose orientation is different from those in adjoining domains. To create two twin meta-grains of fcc lattice (Fig. 2b), a cube of singly oriented fcc lattice was created with its three ⟨001⟩ orientations being parallel to the X, Y and Z axes (Extended Data Fig. 1b, c). The fcc unit cell had lattice constants of 5 mm × 5 mm × 5 mm and struts with diameters of 1 mm. Subsequently, a plane at the centre of the global cube and perpendicular to the X axis was defined as the boundary between two twin meta-grains. Lattices on each side of the boundary were rotated to the same angles but in opposite directions: lattices in the right side of the boundary (Extended Data Fig. 2c) were first rotated anticlockwise by 45° about the X axis (Extended Data Fig. 1d) and then by 45° about the Y axis to generate a meta-grain of fcc lattice. This rotation sequence is shown in Extended Data Fig. 1c–e, where the x'', y'' and z'' axes are the final coordinates of the lattices after the two anticlockwise rotations. By contrast, lattices in the other side were rotated clockwise by 45° about the X axis and then 45° about the Y axis to create the second twinned meta-grain. The two constructed meta-grains are shown in Extended Data Fig. 2a, with the one on the right-hand side highlighted. Because of the globally constrained dimensions (40 mm × 40 mm × 40 mm), the rotation of the lattices caused incomplete unit cells on free surfaces (and at the boundaries between meta-grains; Fig. 2a). This weakened the architected material containing multiple meta-grains with different orientations. A planar lattice frame with a two-dimensional unit cell containing a centred node was introduced to help maintain the connectivity of struts (Extended Data Fig. 2b). The dimensions of the planar unit cell are 5 mm × 5 mm, with a strut diameter of 1 mm. The size of the meta-grains was reduced by further dividing the global cube into smaller meta-grains, that is, increasing the number of meta-grains from two to four, eight, 16, 18 and 27 (Extended Data Fig. 2b–e). Because the user has total control of the design, an architected material containing a given number of meta-grains exhibits highly reproducible behaviour (Extended Data Fig. 3).

We designed a cube (Extended Data Fig. 5) consisting of eight meta-grains separated by incoherent high-angle boundaries to study the role of misorientation on crack propagation (Fig. 2d) and the deformation of lattices in different base materials (Extended Data Fig. 6). All meta-grains had the same size, 20 mm × 20 mm × 20 mm (Extended Data Fig. 5a). The unit cell was fcc with constants of 5 mm × 5 mm × 5 mm and a strut diameter of 1 mm. The cube consisted of two layers, each comprising four meta-grains. In the top layer, the top right meta-grain with the three ⟨001⟩ orientations coinciding with the global X, Y and Z axes (Extended Data Fig. 5b) was chosen as the reference meta-grain. The unit cells of the three neighbouring meta-grains (moving anticlockwise) in the same layer were created by rotating the unit cell of the reference meta-grain by 30°, 45° and 60° about the Z axis (Extended Data Fig. 5b). The reference point of rotation was the centre of the original unit cell. Meta-grains in the bottom layer were created in a similar way, but in a different sequence (Extended Data Fig. 5c), with the aim of increasing the randomness of the misorientation distribution. The outer frame was not introduced to reveal the stopping effect of high-angle boundaries on crack propagation (Fig. 2g).

Mimicking precipitates. Precipitates were mimicked by embedded lattice domains (meta-precipitates) with different lattice parameters from those of the matrix. The lattice parameters (type, spacing and orientation) of meta-precipitates can be tailored to design different degrees of coherency between the precipitates and the matrix. The diameters of strut lattices in meta-precipitates can be varied to mimic an ordered arrangement of atomic bonds, for example, the Ni–Al bonds in γ' in nickel superalloys. The meta-precipitates in Fig. 3c, d were designed by embedding 25 cubic meta-precipitates in an fcc matrix. Meta-precipitates near the free surfaces of the global cube and their locations in the matrix are shown in Extended Data Fig. 7a, b. The ⟨001⟩ orientations of the matrix unit cell were parallel to the global X, Y and Z axes (Extended Data Fig. 7a). The unit cell of the matrix was fcc, with lattice constants of 5 mm × 5 mm × 5 mm and a strut diameter of 1 mm (Extended Data Fig. 7c). Each meta-precipitate had dimensions of 7.5 mm × 7.5 mm × 7.5 mm and was made of a face-centred tetragonal unit cell with lattice constants of 3 mm × 3 mm × 4 mm and a strut diameter of 1 mm (Extended Data Fig. 7d). The lattices of the meta-precipitates were randomly rotated. Frames were introduced as the interfaces between the matrix and precipitates to increase the connectivity of struts across the interfaces.

Mimicking phases. Because a crystal phase is defined by its lattice type, multiple phases can be imitated by assigning different lattice types to different macro-lattice domains. A single fcc (or single fcc) architected phase was generated by an fcc (or bcc) architected unit cell (Extended Data Fig. 9). The global dimensions of the multiple meta-phases was 40 mm × 40 mm × 40 mm. The fcc and bcc unit cells had the same lattice constants (5 mm × 5 mm × 5 mm) and the same strut diameter (1 mm). The mixture of the two fcc and bcc phases consisting of 50 Voronoi meta-grains was designed by filling the 50 meta-grains with the fcc and bcc unit cells (Extended Data Fig. 9c). The global (40 mm × 40 mm × 40 mm) cube comprising the two meta-phases was divided into three layers (top, middle and bottom). Meta-grains in the top and bottom layers were filled by the fcc phase whereas the middle-layer meta-grains were made of the bcc phase: 11 fcc meta-grains for the top layer, 25 bcc meta-grains for the middle layer and 14 fcc meta-grains for the bottom layer. The lattices in all meta-grains were randomly rotated to increase the isotropy of the lattice cube.

Kresling lattice. A Kresling lattice cylinder was constructed to loosely imitate an hcp phase (Extended Data Fig. 10a)[36]. Struts and nodes on the bottom (ABCDEF) and top (A′B′C′D′E′F′) surfaces of the Kresling unit cell formed two regular hexagons that are parallel and equal. Similarly to the terminology in the hcp crystal phase, ABCDEF and A′B′C′D′E′F′ were the two basal planes. The bottom hexagon was created with a side length of 8 mm. Subsequently, the top hexagon A′B′C′D′E′F′ was formed by translating the bottom hexagon along the z axis and then rotating the translated hexagon clockwise by 30° about the z axis (Extended Data Fig. 10a). The angle ∠AOH (with H the midpoint of AF and O the centre of the hexagon) was 30°, making HA′ perpendicular to AF. The c parameter (the length of OO′) of the Kresling hcp unit cell was 8 mm. The unit cell was created by connecting AA′, A′B, BB′, B′C, CC′, C′D, DD′, D′E, EE′, E′F, FF′ and F′A. The Kresling hcp-like phase was built by stacking three Kresling unit cells along the z axis. The total height of the Kresling hcp-like phase was 24 mm, with a strut diameter of 3 mm for AA′, BB′, CC′, DD′, EE′ and FF′ and of 2 mm for the diagonal and basal struts (Extended Data Fig. 10b).

Materials and fabrication. We used various base materials to fabricate designed materials to demonstrate the applicability of our polygrain-inspired approach. The choice of base material was based on the phenomenon of interest. For example, whereas ductile polylactic acid (PLA) polymer and stainless steel (316L) were used to study the shear-band activity, a polymerization resin that is brittle after curing and heat treatment was used to study the crack propagation.

Cubic (except for Fig. 2g) and Kresling lattices were made of PLA filaments and thermoplastic co-polyester (Natural FLEX 45) filaments, respectively. The filaments were provided by RS. Lattices were fabricated by a fused-deposition-modelling Ultimaker 2 printer. Models of designed meta-crystals were sliced into sequential layers by the pre-processing software Cura, with a layer height of 0.1 mm. The nozzle of the printer was heated (to 210 °C for PLA and 215 °C for co-polyester) to melt the filament. The nozzle diameter is 0.4 mm. The molten material was extruded and deposited on a build plate layer-by-layer according to the sliced sequences of the designed lattices. The build platform was heated (to 60 °C for PLA and 100 °C for co-polyester) to increase the bonding between layers. The nozzle speed was 30 mm s^{-1} for PLA and 15 mm s^{-1} for co-polyester.

To study the role of meta-grain boundaries in the propagation of macro-cracks, a single meta-grain and eight meta-grains separated by incoherent high-angle boundaries (Extended Data Fig. 5) were made of a photopolymerization resin (Visijet M2 RWT) provided by 3D Systems. The resin was brittle after curing and subsequent heat treatment. The meta-crystals were printed by a stereolithography printer (ProJet MJP 2500) in which resin is cured by ultraviolet light. Similarly to the fused-deposition-modelling process, meta-crystal models were first sliced into layers of thickness 0.1 mm. The ultraviolet light cured the resin according to the slicing sequence of the models. A wax material was used to support the built lattices, to improve the geometric accuracy and quality of the lattices. The wax was removed from the built lattices by post-treatment in an oven at 60 °C for 5 h.

To study the influence of the base material on the behaviour of polycrystal-like lattices, the eight meta-grains (Extended Data Fig. 5) were fabricated from both the elasto-plastic PLA and the 316L austenitic stainless steel. The PLA was printed by Ultimaker 2 with parameters as above; the steel was fabricated using a Renishaw AM250 printer in argon atmosphere. The dimensions of the eight meta-grains were halved for 316L: global dimensions, 20 mm × 20 mm × 20 mm; size of each meta-grain, 10 mm × 10 mm × 10 mm; lattice constants, 2.5 mm × 2.5 mm × 2.5 mm; and strut diameter, 0.5 mm. A hatch pattern was used for the inner area, with a power intensity of 180 W, a spacing of 150 μm, an exposure time of 110 μs

and a point distance of 65 μm. The outer skin was made by two contours, with a power intensity of 100 W, a spacing of 55 μm, an exposure time of 90 μs and a point distance of 40 μm. The mechanical properties of the PLA and co-polyester filaments, brittle resin and 316L steel are given in Extended Data Table 1.

Microstructure characterization. Scanning electron microscope (SEM) imaging and electron backscatter diffraction (EBSD) were carried out on an austenitic stainless steel (316L) using a Zeiss Auriga SEM at a voltage of 20 kV (Fig. 4e, f). γ/γ' microstructure in a nickel single crystal (with a composition similar to CMSX4) was revealed by chemical etching (2.5% phosphoric acid in methanol solution, applying 10 V for 30 s). The γ/γ' microstructure (Fig. 4h) was observed using the SEM Sigma300 at a voltage of 10 kV.

Mechanical tests and analyses. We studied the mechanical properties of all macro-lattices by using compression tests carried out by a 100-kN Zwick machine using displacement control at a strain rate of 10^{-3} s^{-1} at room temperature. To minimize the effect of friction, the top and bottom compression plates were lubricated with dry molybdenum disulfide. The loading direction was parallel to the build direction (the *Z* direction) of the prints. Stresses were calculated by dividing the recorded forces by the nominal area of the section that was perpendicular to the *Z* direction. Engineering strains were derived by dividing the change in length along the *Z* direction by the initial length (40 mm for the polymer lattice cubes and 24 mm for the Kresling lattice). The size of a designed meta-grain was calculated as the diameter of a sphere that has approximately the same volume as the designed meta-grain. The compression tests of meta-crystals were recorded by a Nikon D7100 camera with 200-mm Nikkor macro-lenses for taking images for post-test analyses, and a Canon SX210 for recording videos. Images were characterized by digital image correlation using the commercial software DaVis. The resolution of the analysed image was 6,000 × 4,000 pixels. The subset dimensions used in the digital image correlation analysis were 101 × 101 pixels, with a step size of 25 pixels. We wrote Matlab subroutines to analyse the stress–strain behaviour of the tested lattices. We fitted a linear function over different ranges of the most linear part (up to 2% strain) of a stress–strain curve to identify the elastic modulus. The yield strength was defined as the stress corresponding to the 0.2% strain offset of the fitting line.

Finite-element analysis. We used FEM to simulate the deformation of macro-lattices. Models of macro-lattices generated by the software nTopology Element were imported to Abaqus for FEM simulations. The quasi-static compression of a macro-lattice was modelled using two displacement-controlled rigid-body plates. The first rigid-body plate was fixed underneath the macro-lattice with an encastre boundary condition. The second rigid-body plate was used to compress the macro-lattice with a displacement boundary condition. We used the General Contact algorithm in Abaqus to simulate the interactions between all surfaces, with a penalty friction coefficient of 0.1 and 'hard' pressure–overclosure surface behaviour defined. Macro-lattices were meshed using ten-node quadratic tetrahedral elements (C3D10) with isotropic elastic–plastic material behaviour defined according to the mechanical behaviour data in Extended Data Table 1. Because of the symmetry and periodicity of the arrangement of unit cells in the twin meta-grains, we constructed a reduced finite-element model of the twin meta-grains. This model consisted of the twin boundary and 3 × 3 unit cells in each meta-grain and was constructed using 1,184,608 elements. The Kresling lattice was built using 140,120 elements. The rigid-body plates were meshed using four-node bi-linear quadrilateral elements (R3D4).

Data availability

The datasets generated and analysed during this study are available from the corresponding author on reasonable request.

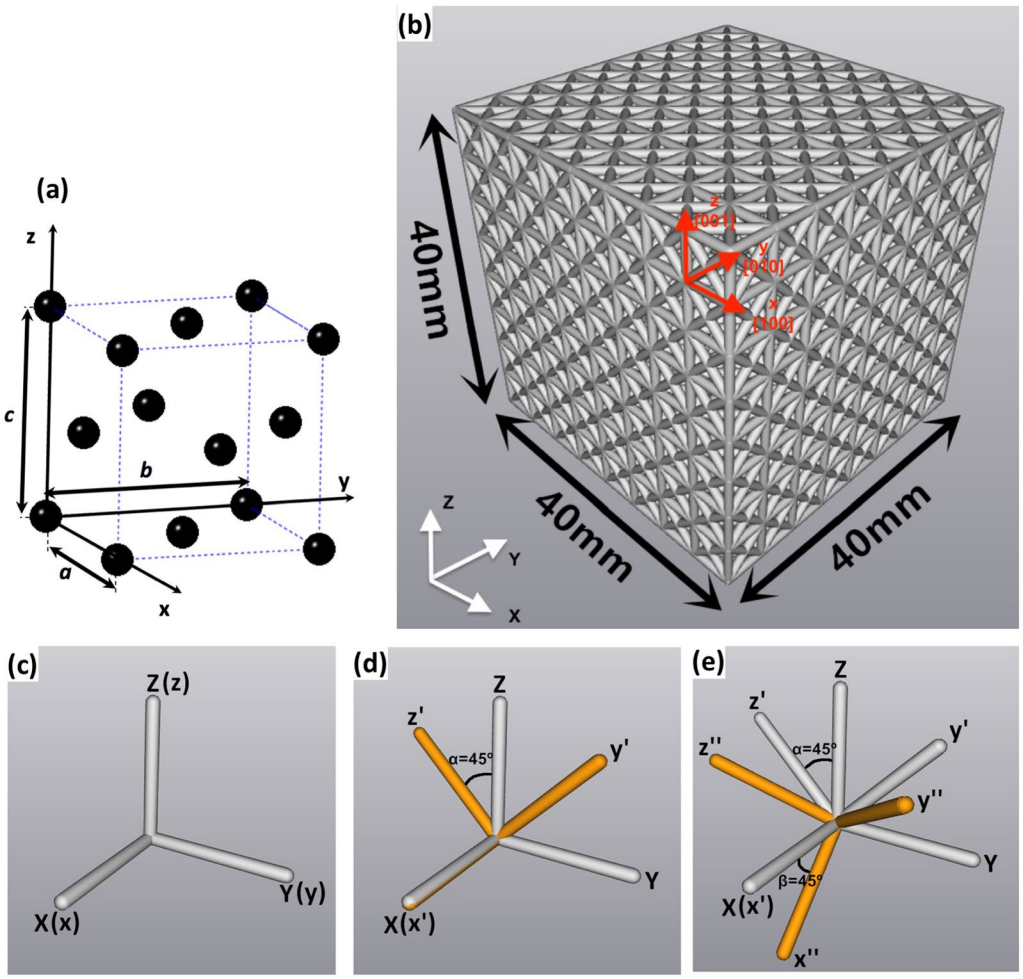

Extended Data Fig. 1 | Mimicking a crystal lattice. a, Unit cell of the fcc lattice. **b**, A macro-lattice cube consisting of 8 × 8 × 8 macro-unit cells. **c**–**e**, The rotation sequence to form a twin meta-grain.

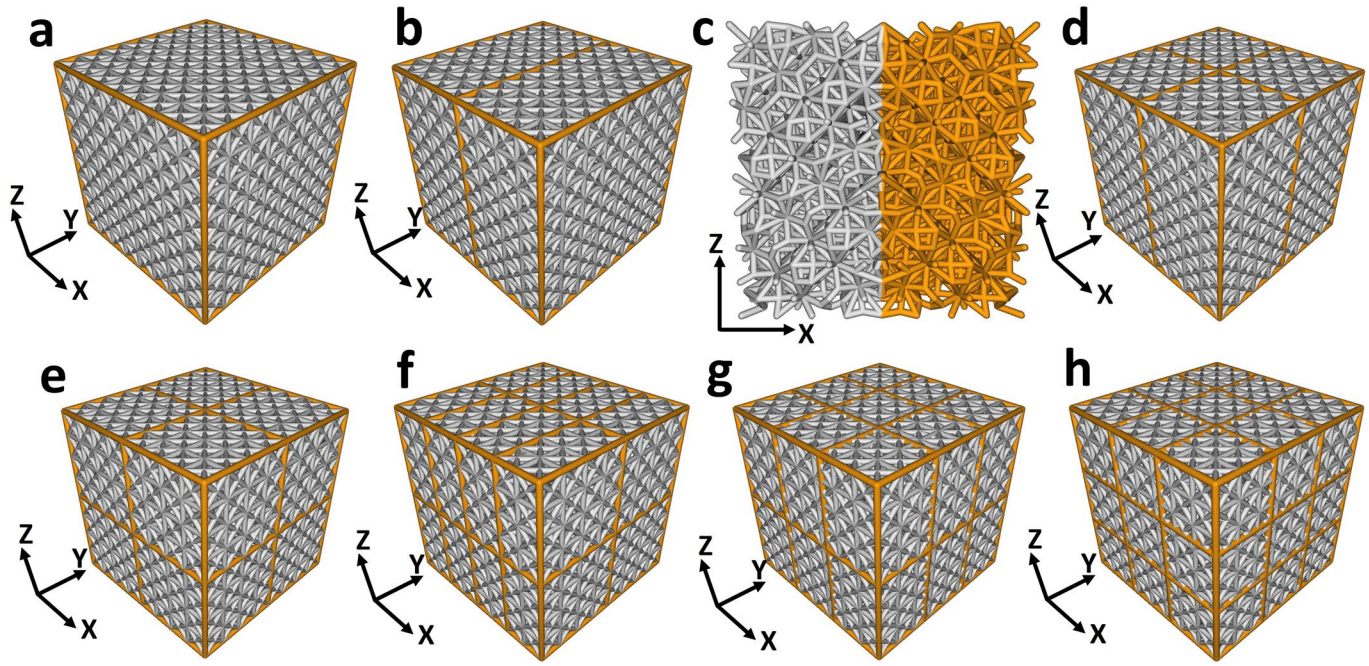

Extended Data Fig. 2 | Different numbers of meta-grains within the same global volume (40 mm × 40 mm × 40 mm). a, A single meta-grain. **b**, **c**, Two twinned meta-grains, with (**b**) and without (**c**) the outer frame. **d**–**h**, Four (**d**), eight (**e**), 16 (**f**), 18 (**g**) and 27 (**h**) meta-grains. The locations of the boundaries are highlighted.

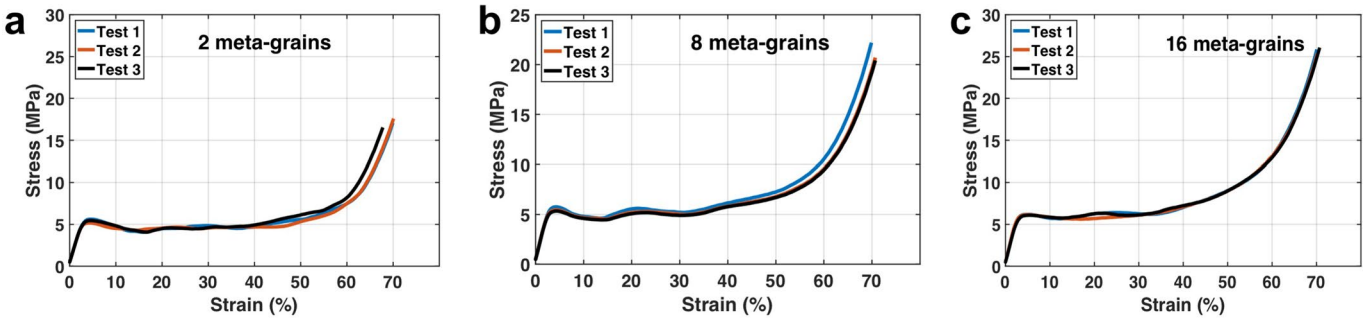

Extended Data Fig. 3 | Repeatability of the mechanical behaviour of architected materials. a–c, Materials consisting of two (**a**), eight (**b**) and 16 (**c**) meta-grains.

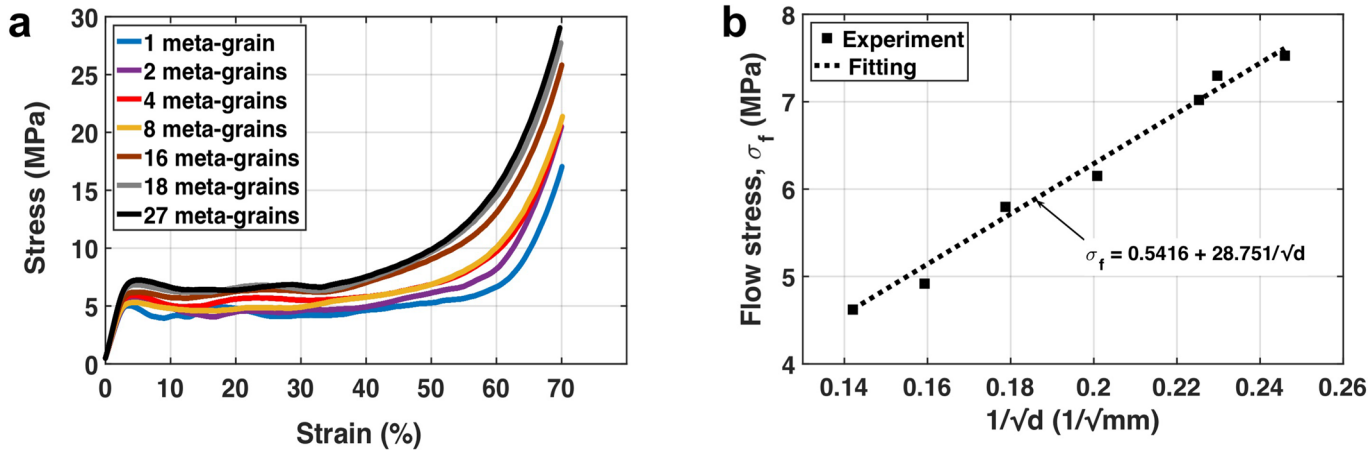

Extended Data Fig. 4 | Effect of meta-grain size on mechanical strength. **a**, Stress–strain curves of architected materials consisting of different numbers of meta-grains. **b**, The flow stress σ_f of architected materials containing meta-grains at a given nominal strain of 40% increases as the size of the meta-grains decreases.

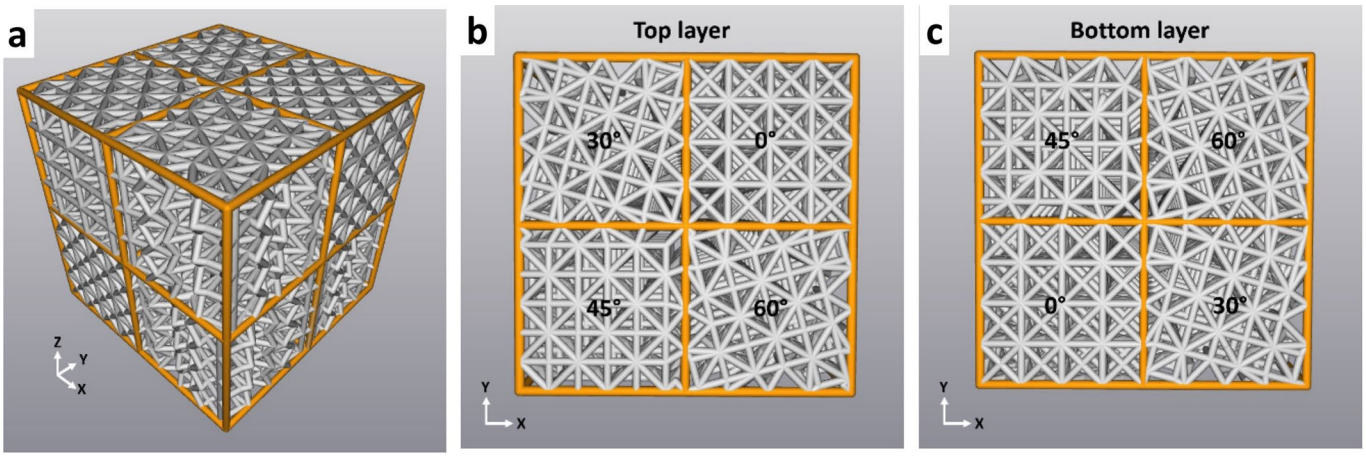

Extended Data Fig. 5 | Mimicking crystalline grains separated by incoherent high-angle boundaries. a, Model of eight meta-grains. **b**, **c**, The orientations of lattices (with respect to the global *X*, *Y* and *Z* co-ordinates) in the four meta-grains in the top (**b**) and bottom (**c**) layers.

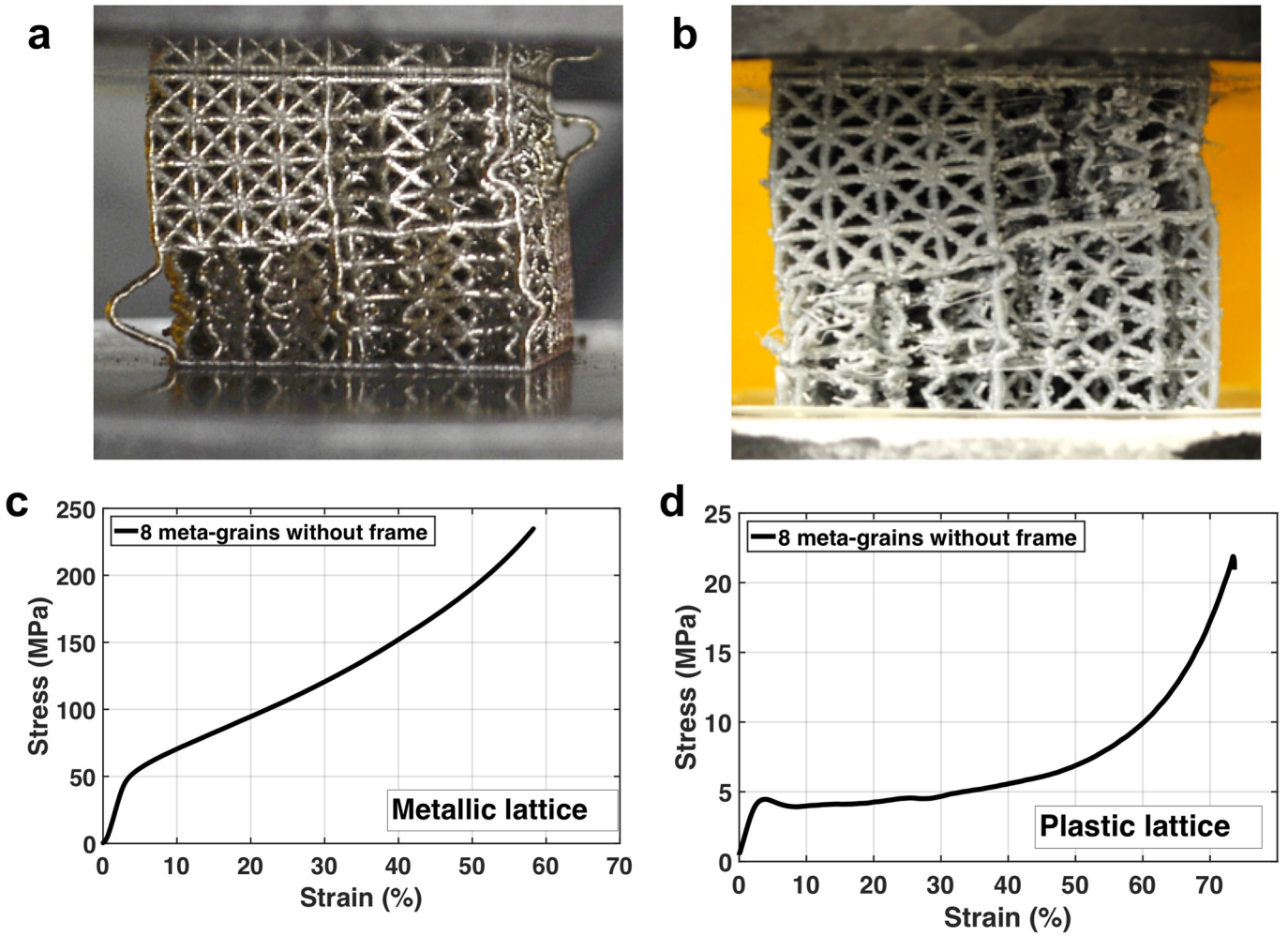

Extended Data Fig. 6 | Deformation behaviour of an architected material containing eight meta-grains separated by incoherent high-angle boundaries. a, **b**, Macro-lattice fabricated from 316L stainless steel (**a**) and an elasto-plastic polymer (**b**). **c**, **d**, Stress–strain constitutive behaviour of the macro-lattices fabricated from the steel (**c**) and polymer (**d**).

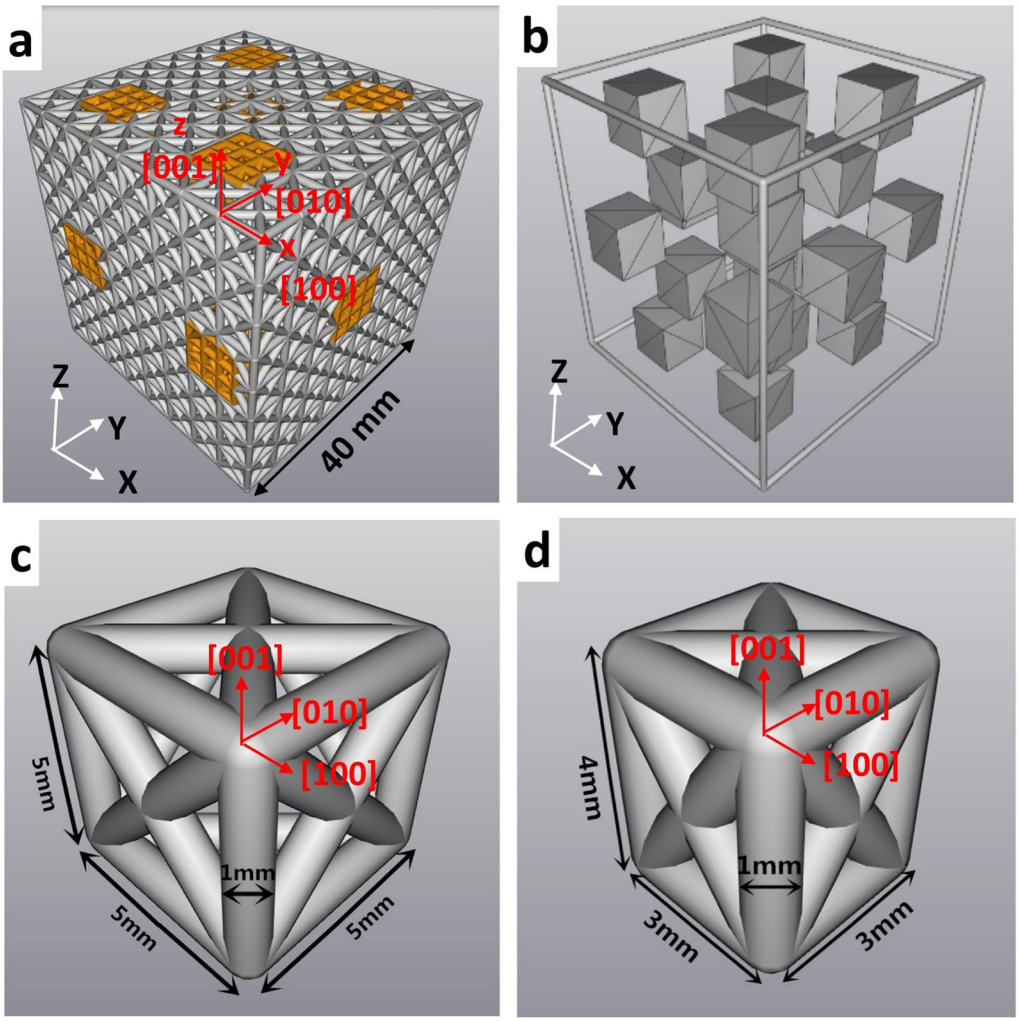

Extended Data Fig. 7 | Mimicking precipitates. a, Meta-precipitate lattice (orange) embedded in the matrix. **b**, Cubic morphology and locations of meta-precipitates inside the fcc meta-phase. **c**, fcc unit cell of the matrix. **d**, Face-centred tetragonal unit cell of the meta-precipitate.

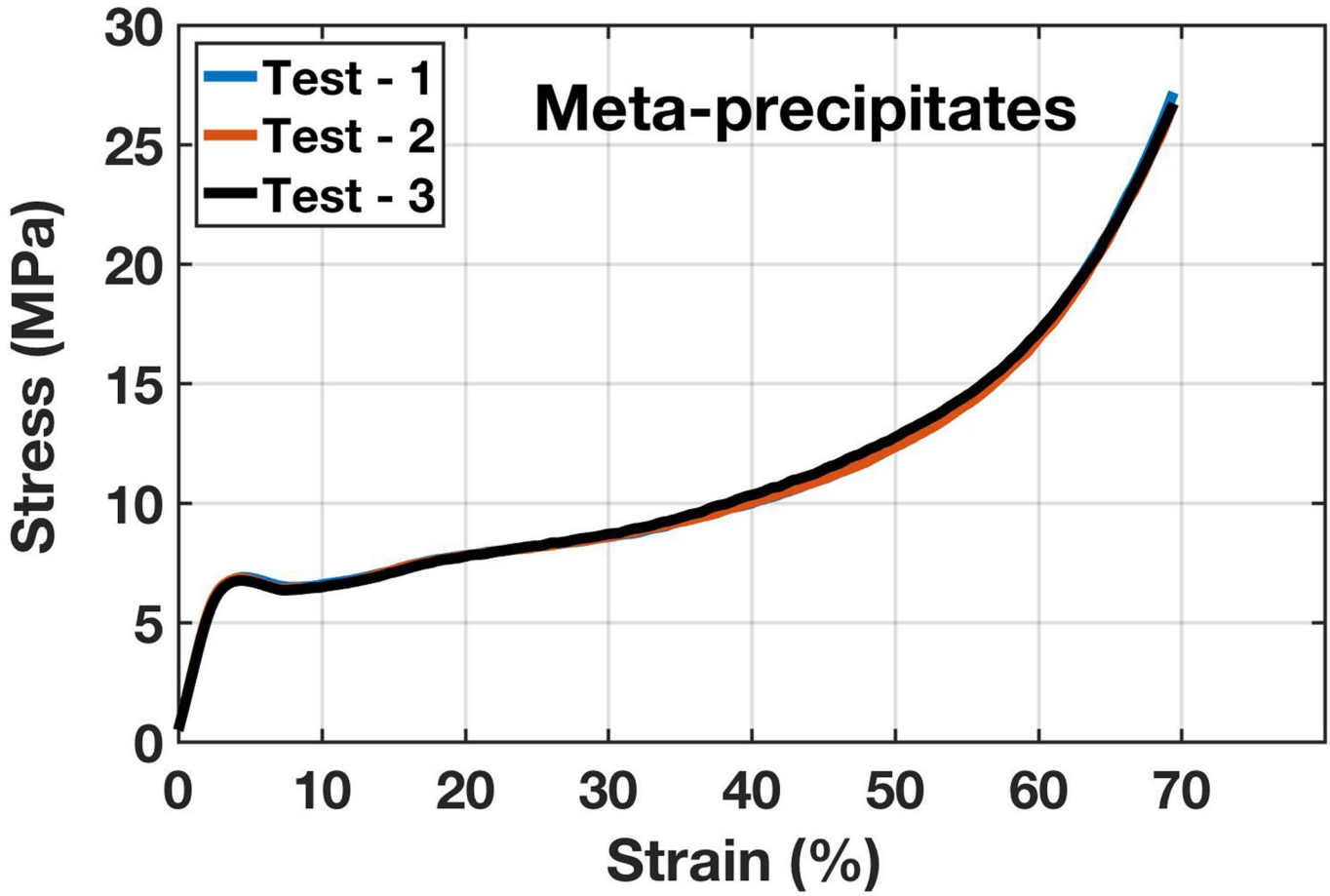

Extended Data Fig. 8 | Repeatability of the mechanical behaviour of an architected material. This material contains 25 meta-precipitates.

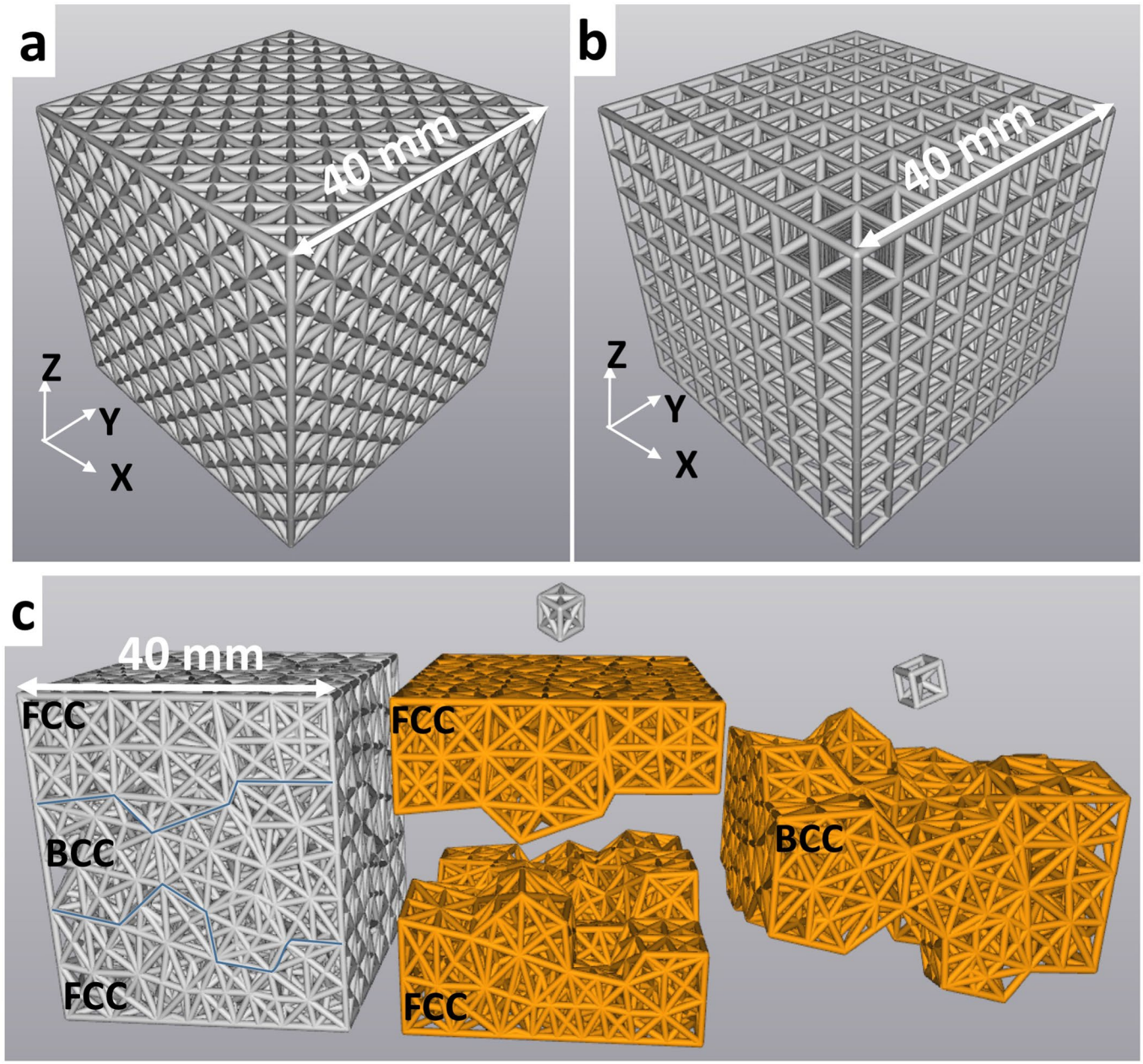

Extended Data Fig. 9 | Mimicking multiple phases. a, Single fcc-phase meta-grain. **b**, Single bcc-phase meta-grain. **c**, A cube of meta-polygrains (left panel) consisting of two meta-phases: fcc (top and bottom layers; middle panel) and bcc (middle layer; right panel).

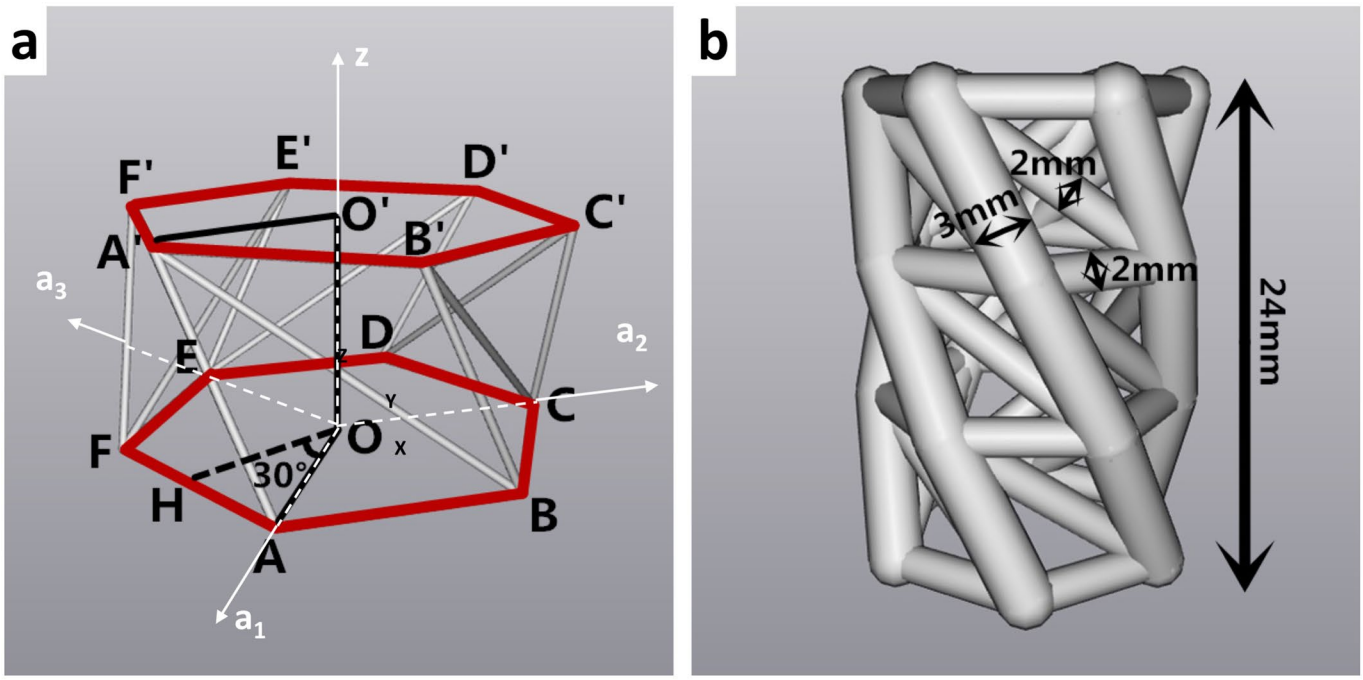

Extended Data Fig. 10 | Kresling lattice. a, Unit cell. **b**, hcp-inspired meta-phase.

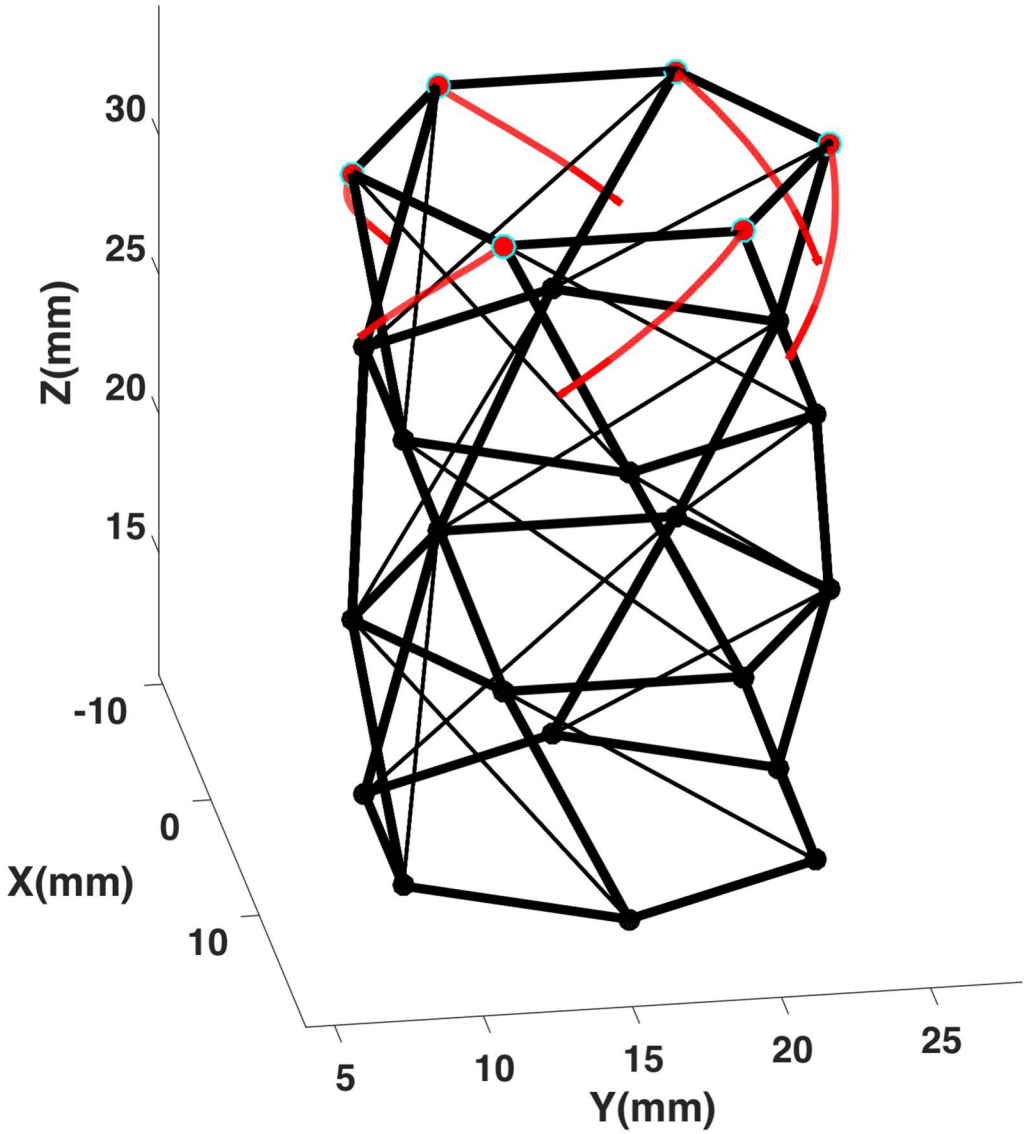

Extended Data Fig. 11 | Helical movement changes the stack sequence of nodes. Red lines represent the helical movements of basal nodes; for clarity, only the movement of basal nodes on the top plane are shown.

Extended Data Table 1 | Mechanical properties of base materials

	Tensile modulus (MPa)	Tensile strength (MPa)	Elongation (%)
Ductile PLA*	3,310	110	160
Resin*	1,000 - 1,600	37 - 47	7 - 16
Natural FLEX 45*	95	24	530
316L**	185,000 – 200,000	585	40 - 50

*Data provided by RS and 3D Systems.
**Data obtained from three tensile tests of solid cylindrical samples (fabricated by powder-bed selective laser fusion) at room temperature and a strain rate of 10^{-3} s^{-1}.